J. Fluid Mech. (2009), *vol.* 625, *pp.* 75–96.
doi:10.1017/S0022112008005454 Printed in the United Kingdom

Interacting oscillatory boundary layers and wall modes in modulated rotating convection

A. RUBIO[1], J. M. LOPEZ[1]† AND F. MARQUES[2]

[1]Department of Mathematics and Statistics, Arizona State University, Tempe, AZ 85287, USA

[2]Departament de Física Aplicada, Universitat Politècnica de Catalunya, Barcelona 08034, Spain

(Received 24 April 2008 and in revised form 4 December 2008)

Thermal convection in a rotating cylinder near onset is investigated using direct numerical simulations of the Navier–Stokes equations with the Boussinesq approximation in a regime dominated by the Coriolis force. For thermal driving too small to support convection throughout the entire cell, convection sets in as alternating pairs of hot and cold plumes in the sidewall boundary layer, the so-called wall modes of rotating convection. We subject the wall modes to small amplitude harmonic modulations of the rotation rate over a wide range of frequencies. The modulations produce harmonic Ekman boundary layers at the top and bottom lids as well as a Stokes boundary layer at the sidewall. These boundary layers drive a time-periodic large-scale circulation that interacts with the wall-localized thermal plumes in a non-trivial manner. The resultant phenomena include a substantial shift in the onset of wall-mode convection to higher temperature differences for a broad band of frequencies, as well as a significant alteration of the precession rate of the wall mode at very high modulation frequencies due to the mean azimuthal streaming flow resulting from the modulations.

1. Introduction

Rayleigh–Bénard convection has long been a popular nonlinear system which is used to study the effects of temporal forcing of the control parameters. Recently, there has been specific interest in how the system responds to a modulated rotation (Bhattacharjee 1990; Niemela, Smith & Donnelly 1991; Thompson, Bajaj & Ahlers 2002). In the laboratory experiments of Thompson *et al.* (2002), the mean rotation rates were restricted to being small enough to ensure that in the unmodulated case the onset of convection was to a bulk mode rather than a wall mode (Ecke, Zhong & Knobloch 1992; Goldstein *et al.* 1993). In numerically reproducing the experimental observations of Thompson *et al.* (2002), Rubio, Lopez & Marques (2008) showed that the oscillatory boundary layers resulting from the modulation greatly affect the Küppers–Lortz spatio-temporal chaos associated with the onset of bulk convection (Küppers & Lortz 1969; Herrmann & Busse 1993; Kuo & Cross 1993; Knobloch 1998; Bodenschatz, Pesch & Ahlers 2000), leading to the experimentally observed spiral and target patterns, even for small amplitude modulations. The secondary flows associated with the oscillatory boundary layers were found to be strongest near the cylinder sidewall, and it is natural to ask how these boundary layers interact with the much simpler case of wall-localized convection found near onset at higher mean rotation rates.

† Email address for correspondence: lopez@math.la.asu.edu

Preliminary numerical experiments showed that modulations of the rotation rate could delay the onset of thermal convection to thermal forcing levels well beyond those required in the unmodulated case. Or, to put it another way, with modulated rotation the three-dimensional wall modes could be driven to an axisymmetric state with a greatly reduced heat flux, a behaviour we refer to as quenching. The focus of the present study is the examination of how the wall modes are quenched as a function of modulation amplitude and modulation frequency. For the most part, we hold the thermal forcing constant to see how a single initial wall-mode state either persists or is driven to a state without thermal convection. This focused approach permits an extensive survey of modulation amplitudes and modulation frequencies and led to the discovery of a wide band of modulation frequencies which quenches thermal convection at even quite modest modulation amplitudes of less than 1 % of the mean rotation rate. Particular attention is given to the interaction between the wall modes of convection and the modulation-driven boundary layers, whose nature changes considerably at high background rotation rates. The modulation-driven secondary flow exists for all non-zero modulation amplitudes and grows in strength with increasing modulation amplitude and frequency. As such, it is surprising that the optimal modulation frequency for quenching thermal plumes is not associated with frequencies for which the secondary flow is strongest. In fact, at the highest frequencies considered the spatial structure of the thermal plumes remains intact for the range of modulation amplitudes considered. The structure of the mean component of the secondary flow is examined in detail and its interaction with the thermal plumes is discussed. The generation of a streaming flow driven by oscillatory viscous boundary layers is a common phenomenon in parametrically forced fluid dynamics, first elucidated by Schlichting (1932) (also see the review article by Riley 2001). However, in those examples the streaming flow is normal to the direction of the oscillations. In our problem, the imposed oscillations are in the azimuthal direction and a meridional (normal to the azimuthal direction) streaming flow is also established, but so is a streaming flow in the azimuthal direction. Both streaming flows have important effects. The azimuthal streaming flow decreases the precession rate of the wall modes at high frequency, while the meridional streaming flow drives a non-trivial mean temperature perturbation at the frequencies where the quenching takes place.

The layout of the paper consists of a description of the governing equations, boundary and initial conditions and the spectral method used to solve them in § 2. A brief overview of wall-mode convection in rotating cylinders is presented in § 3 in order to provide a setting for the new results due to the harmonic modulation, presented in § 4. Section 4 consists of a number of subsections; § 4.1 presents the main motivating observation for the paper – the quenching of the wall modes with a small amplitude modulation at intermediate frequencies. Section 4.2 explores the physical mechanism responsible for the quenching – the action of the oscillatory boundary layers – in a regime where the wall modes are not present. Finally, § 4.3 examines the structure and behaviour of the modulated wall modes, the states that result from the competition between the wall-localized thermal convection and the modulation-driven flow in regimes where the thermal convection is not quenched.

2. Governing equations and numerical technique

Consider the flow in a rotating circular cylinder, with no-slip boundary conditions, of radius r_0 and depth d, with a modulated angular frequency $\omega(t^*) = \omega_0 + \omega_1 \sin(\omega_m t^*)$,

where t^* is dimensional time. The endwalls are maintained at constant temperatures, $T_0 - \Delta T/2$ at the top and $T_0 + \Delta T/2$ at the bottom, and the sidewall is insulating. The Boussinesq approximation is implemented, treating all fluid properties as constant except for the density in the gravitational term, which varies linearly with temperature. The centrifugal buoyancy (Lopez, Rubio & Marques 2006; Marques *et al.* 2007) is ignored in this study as the majority of related experiments in rotating convection have very small Froude numbers (typically $Fr = \omega_0^2 r_0/g < 0.025$, where g is the gravitational acceleration in the negative z-direction). Nevertheless, in any physical experiment $Fr \neq 0$ and so comparing the present results with experiments needs to be done with caution. The system is non-dimensionalized using d as the length scale, d^2/ν as the time scale (ν is the kinematic viscosity), $\nu^2\rho_0/d^2$ as the pressure scale (ρ_0 is the density at mean temperature T_0) and ΔT (the difference in temperature between the top and bottom) as the temperature scale. In a frame of reference rotating at the mean rotation rate ω_0, the non-dimensional governing equations are

$$(\partial_t + \boldsymbol{u}\cdot\nabla)\boldsymbol{u} = -\nabla p + \nabla^2\boldsymbol{u} + \frac{Ra}{\sigma}(\Theta - z)\boldsymbol{z} + 2\Omega_0\boldsymbol{u}\times\boldsymbol{z}, \tag{2.1}$$

$$(\partial_t + \boldsymbol{u}\cdot\nabla)\Theta = w + \sigma^{-1}\nabla^2\Theta, \qquad \nabla\cdot\boldsymbol{u} = 0, \tag{2.2}$$

where $\boldsymbol{u} = (u, v, w)$ is the velocity in cylindrical coordinates (r, θ, z), P is the dynamic pressure, $\boldsymbol{z}$ is the vertical unit vector in the z-direction and Θ is the temperature deviation with respect to the conductive linear temperature profile; the relationship between Θ and the non-dimensional temperature T is given by

$$T = T_0/\Delta T - z + \Theta, \tag{2.3}$$

where $T_0/\Delta T - z$ is the conductive temperature profile.

There are six independent non-dimensional parameters:

Rayleigh number:	$Ra = \alpha g d^3 \Delta T/\kappa\nu$,
Coriolis number:	$\Omega_0 = \omega_0 d^2/\nu$,
Prandtl number:	$\sigma = \nu/\kappa$,
aspect ratio:	$\gamma = r_0/d$,
modulation amplitude:	$\Omega_1 = \omega_1 d^2/\nu$,
modulation frequency:	$\Omega_m = \omega_m d^2/\nu$,

where α is the coefficient of volume expansion and κ is the thermal diffusivity. The boundary conditions (in a frame of reference rotating at the mean rotation rate ω_0) are

$$\begin{aligned} r = \gamma: &\quad \Theta_r = u = w = 0, \quad v = \gamma\Omega(t) \\ z = \pm 0.5: &\quad \Theta = u = w = 0, \quad v = r\Omega(t), \end{aligned}$$

where $\Omega(t) = \Omega_1 \sin(\Omega_m t)$ is the angular velocity of the cylinder in a reference frame rotating with the mean angular velocity Ω_0. To simplify the discussion, we introduce the relative modulation amplitude $A = \Omega_1/\Omega_0$ to allow for comparison between states with differing Ω_0. A will be used instead of Ω_1, except in the particular case when $\Omega_0 = 0$, as A is then not defined.

The governing equations and boundary conditions are invariant under arbitrary rotations through angle α about the axis R_ϕ, whose action is

$$R_\phi(u, v, w, \Theta)(r, \theta, z, t) = (u, v, w, \Theta)(r, \theta + \phi, z, t). \tag{2.4}$$

They are also reflection symmetric about the cylinder half-height. The action K_z of this so-called Boussinesq symmetry is

$$K_z(u, v, w, \Theta)(r, \theta, z, t) = (u, v, -w, -\Theta)(r, \theta, -z, t). \tag{2.5}$$

The symmetry group of the system is $\mathcal{G} = SO(2) \times Z_2$, with $SO(2)$ generated by R_α and Z_2 by K_z.

The governing equations are solved using the second-order time splitting of Hughes & Randriamampianina (1998), combined with a pseudo-spectral method for the spatial discretization, utilizing a Galerkin–Fourier expansion in the azimuthal coordinate θ and Chebyshev collocation in r and z. Following Orszag & Patera (1983), we have used the combinations $u_+ = u + \mathrm{i}v$ and $u_- = u - \mathrm{i}v$ in order to decouple the linear diffusion terms in the momentum equations. For each Fourier mode, the resulting Helmholtz equations for Θ, w, u_+ and u_- have been solved using a diagonalization technique in the two coordinates r and z. The coordinate singularity at the axis ($r = 0$) is treated following the prescription in Fornberg (1998) that guarantees the regularity conditions at the origin needed to solve the Helmholtz equations (Mercader, Net & Falqués 1991).

The code has been validated on a number of convection problems in rotating cylinders (Lopez *et al.* 2006, 2007; Marques *et al.* 2007; Rubio *et al.* 2008), establishing resolution requirements over a wide range of parameters. For the cases considered in this paper, $n_r = 48$ and $n_z = 24$ Chebyshev modes in r and z, respectively, were employed. For cases where the solution is non-axisymmetric, $n_\theta = 184$ Fourier modes in θ were used. The time discretization used $\delta t \leqslant 0.00015$ viscous time units, with no fewer than 300 δt per modulation period. Figure 1 shows the rate of spectral convergence of Θ for a typical modulated wall mode, with $A = 0.0075$, $\Omega_m = 10^{1.5}$ and $Ra = 5 \times 10^4$, computed with $(n_r, n_z, n_\theta) = (48, 24, 184)$ (filled symbols), and compared to a simulation with higher resolution using $(n_r, n_z, n_\theta) = (96, 48, 184)$ (open symbols). The temperature perturbation is expanded as

$$\Theta(r, \theta, z, t) = \sum_{m=0}^{2n_r+1} \sum_{n=0}^{n_z} \sum_{k=-n_\theta/2}^{n_\theta/2-1} \hat{v}_{mnk}(t) T_m(r/\gamma) T_n(2z) \mathrm{e}^{\mathrm{i}k\theta}. \tag{2.6}$$

Although the radial sum extends up to $2n_r + 1$, Fornberg's prescription guarantees that there are exactly $n_r + 1$ degrees of freedom in the radial direction. To demonstrate the spectral convergence of the method, the temperature perturbation was separated into its radial, axial and azimuthal components:

$$\Theta_m(r, \theta, z, t) = \sum_{n=0}^{n_z} \sum_{k=-n_\theta/2}^{n_\theta/2-1} \hat{v}_{mnk}(t) T_m(r/\gamma) T_n(2z) \mathrm{e}^{\mathrm{i}k\theta}, \tag{2.7}$$

$$\Theta_n(r, \theta, z, t) = \sum_{m=0}^{2n_r+1} \sum_{k=-n_\theta/2}^{n_\theta/2-1} \hat{v}_{mnk}(t) T_m(r/\gamma) T_n(2z) \mathrm{e}^{\mathrm{i}k\theta}, \tag{2.8}$$

$$\Theta_k(r, \theta, z, t) = \sum_{m=0}^{2n_r+1} \sum_{n=0}^{n_z} \hat{v}_{mnk}(t) T_m(r/\gamma) T_n(2z) \mathrm{e}^{\mathrm{i}k\theta}. \tag{2.9}$$

The relative truncation error was estimated for the radial and axial Chebyshev expansions by dividing the largest L_2-norm component of the lower resolution solution

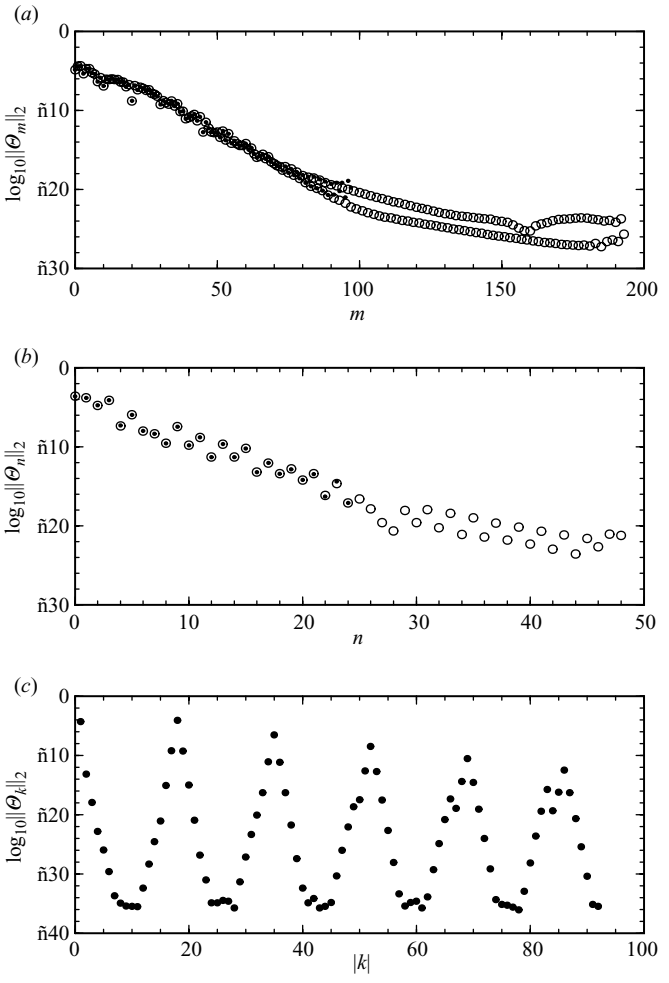

FIGURE 1. The L_2-norms of (*a*) Θ_m, (*b*) Θ_n and (*c*) Θ_k for a modulated wall mode at $A = 0.0075$, $\Omega_m = 10^{1.5}$, with $Ra = 5 \times 10^4$ and $\Omega_0 = 625$. The open symbols correspond to solutions obtained using $(n_r, n_z, n_\theta) = (96, 48, 184)$, while the filled symbols correspond to solutions with $(n_r, n_z, n_\theta) = (48, 24, 184)$.

by the smallest L_2-norm component of the same, where the L_2-norm is given by

$$||\Theta||_2 = \left[\int_{-1/2}^{1/2}\int_0^{2\pi}\int_0^{\gamma} \Theta^2(r,\theta,z) r \,\mathrm{d}r \,\mathrm{d}\theta \,\mathrm{d}z\right]^{1/2}. \tag{2.10}$$

In the azimuthal direction, the relative truncation error was estimated by considering the ratio of the peak of the first harmonic to that of the fifth harmonic. The relative truncation error for the solution shown in figure 1 is 10^{-15} in r, 10^{-13} in z and 10^{-8} in θ.

In the present study, the aspect ratio $\gamma = 4$, Prandtl number $\sigma = 7$ and Coriolis number $\Omega_0 = 625$ are fixed to correspond to those in previous studies (Lopez *et al.* 2006, 2007), and we consider variations in A and Ω_m for $Ra = 4 \times 10^4$ and 5×10^4.

FIGURE 2. Isosurfaces of Θ, at $\Theta = \pm 0.05$, for $m = 17$ wall mode at $Ra = 5 \times 10^4$, $\Omega_0 = 625$ and $A = 0$. Movie 1, available in the online version, shows this solution over seven viscous times at a rate of 0.84 viscous times per second.

3. Background on unmodulated wall modes

For the constant rotation problem in the limit of zero centrifugal force, the basic state consists of solid-body rotation with the conductive linear temperature profile,

$$(u, v, w, \Theta)(r, \theta, z, t) = (0, 0, 0, 0). \tag{3.1}$$

For small Ω_0 (between about 20 and 100, depending on the parameter regime), convection sets in as a bulk mode with Küppers–Lortz spatio-temporal chaos. For $\Omega_0 > 125$ and $\sigma = 6.4$, the onset of convection occurs as a wall mode, a convective mode local to the sidewall emerging as a result of the interplay between the Coriolis force and the sidewall (Zhong, Ecke & Steinberg 1991; Goldstein *et al.* 1994). The onset of the wall mode breaks the continuous $SO(2)$ symmetry of the basic state; the wall modes are invariant to discrete rotations $R_{2\pi/m}$ where the azimuthal wavenumber m is the number of pairs of hot and cold plumes. Breaking the $SO(2)$ symmetry leads to a precession of the wall-mode structure (Ecke *et al.* 1992). The spatial structure does not vary in time, the solution is a rotating wave and hence a relative equilibrium in a frame of reference rotating at its precession frequency. The K_z reflection symmetry is also broken, but the wall modes are invariant under a half-wavelength rotation composed with a reflection $R_{\pi/m}K_z$.

For $\Omega_0 = 625$, $\sigma = 7$ and $\gamma = 4$, the emergence of the wall mode has been studied in some detail (Lopez *et al.* 2007). Onset is via an Eckhaus–Benjamin–Feir instability in which the solution with $m = 18$ bifurcates first at $Ra = 42\,286$, and $m = 17$ mode bifurcates and becomes stable to long-wave perturbations at a slightly larger Ra. The onset of convection throughout the cell, i.e. the onset of bulk convection, occurs at about $Ra = 9.6 \times 10^4$, with some considerable influence from initial conditions (Marques & Lopez 2008). For the majority of this study, $m = 17$ wall mode at $Ra = 5 \times 10^4$ (shown in figure 2 and movie 1, available in the online version), was used as the initial condition since the dynamics of the modulated wall modes of various wavenumbers were found to be qualitatively the same. The instantaneous

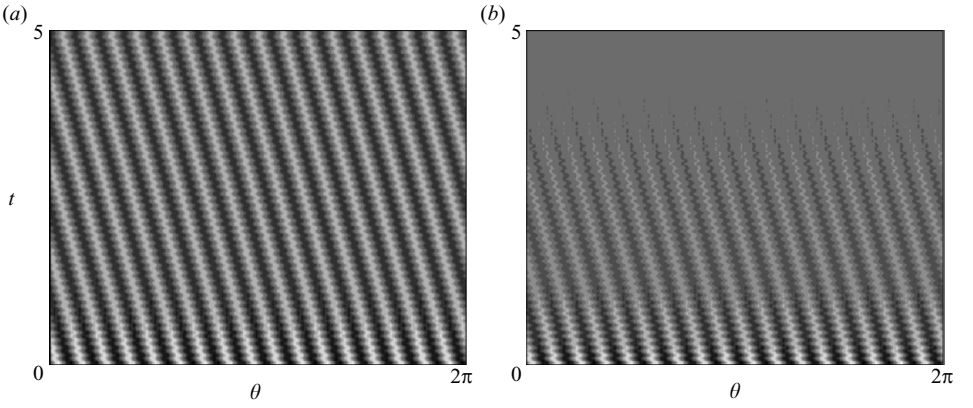

FIGURE 3. Space–time diagrams ($\theta \in [0, 2\pi)$ in the horizontal direction and five viscous times in the vertical direction) of $\Theta(r = \gamma, \theta, 0, t)$ for modulated wall modes at $Ra = 5 \times 10^4$, $\Omega_0 = 625$, $\Omega_m = 10^{1.75}$ with (*a*) $A = 0.0075$ and (*b*) $A = 0.01$. Movies 2 and 3, available in the online version show three-dimensional renderings of these two solutions over five viscous times at a rate of 0.112 viscous times per second, i.e. one modulation period per second.

precession rate of a rotating wave is given by

$$\Omega_p = \frac{\mathrm{d}\phi}{\mathrm{d}t} = \Omega_H / m, \tag{3.2}$$

where ϕ is the angular position of a point in the pattern and Ω_H is the Hopf frequency of the wall mode. For the case shown in figure 2, $\Omega_p = -0.2831$ (it is negative because the precession is retrograde).

4. Results

4.1. *Wall-mode quenching*

When wall modes are subjected to modulated rotation, the convective plumes disappear for quite small amplitudes of modulation over a range of modulation frequencies. While at first glance one may expect resonances to be responsible, they are not. The quenching of the wall mode is not a result of resonance with the modulation-driven flow. The reason is that for there to be a resonance between the two flows, both the temporal frequencies and the spatial frequencies need to be in the same rational ratio (see the discussion in the appendix of Lopez & Marques 2004). While the temporal frequencies could be tuned, the azimuthal wavenumbers are never resonant with them. The wall mode has $m \neq 0$ (here we focus on $m = 17$) and the modulation-driven flow is axisymmetric with $m = 0$.

The space–time plots in figure 3 show the decay of transients for two small modulation amplitudes, $A = 0.0075$ and 0.0100. Both evolutions were initiated with the wall mode shown in figure 2 at $Ra = 5 \times 10^4$, $\Omega_0 = 625$ and $\Omega_m = 10^{1.75}$. This value of Ω_m corresponds to a modulation period of $\tau = 2\pi/\Omega_m \approx 0.112$ viscous times, which is very small compared to the 22.19 viscous times for the unmodulated wall mode to precess 2π radians (the modulation can be seen as 'wiggles' in the mean precession of the wall plumes in the figure). For a modulation amplitude of 0.75 % of the background rotation rate ($A = 0.0075$), we see in figure 3(*a*) that the wall mode quickly adjusts to the modulated rotation rate and persists indefinitely, sloshing back and forth with the modulation period. The adjustment is seen as a reduction in

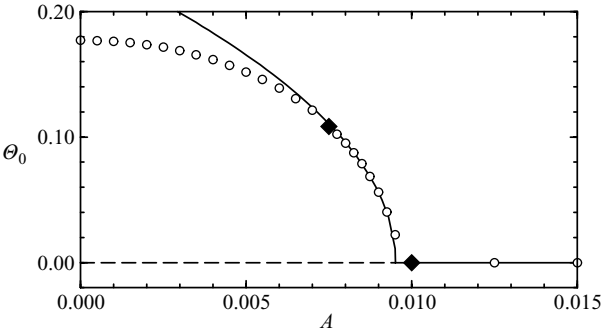

FIGURE 4. Variation of Θ_0 with A at $\Omega_m = 10^{1.75}$. Data points are shown as circles while the cases in figures 3(a) and 3(b) are shown as filled diamonds. A solid black curve shows a quadratic fit of the first five data points while horizontal dashed and solid lines show the values of A for which the synchronous state is unstable and stable, respectively.

contrast of the grey scales over the first viscous time in figure 3(a). Such states where the wall mode coexists with the secondary flow driven by the modulated rotation are referred to as modulated wall modes. These states have the same spatial symmetries as the unmodulated wall modes, however their spatial structure varies with time and they are no longer relative equilibria. For a slightly larger $A = 0.01$, we see from figure 3(b) that in about five viscous times, corresponding to about 45 modulation periods, the wall mode has been quenched and thermal convection ceases. The final state is τ-periodic (synchronous with the modulation) and invariant under both R_α and K_z; we refer to such states as the synchronous states. Movies 2 and 3 in the online version show three-dimensional renderings of the solutions in figures 3(a) and 3(b), respectively.

The quenching of a wall mode at some critical A and Ω_m is a $SO(2) \times Z_2$ symmetry-restoring Hopf bifurcation. A convenient measure to determine when this occurs is the maximum value of Θ at mid-height on the wall:

$$\Theta_{max}(t) = \max_{\theta \in [0,2\pi)} |\Theta(r = \gamma, \theta, z = 0, t)|. \tag{4.1}$$

Its value at the start of a modulation period, $\Theta_{max}(n\tau)$, for n (number of modulation periods) large enough so that the transients have decayed, is constant and we shall denote it as Θ_0. For the synchronous states, when the wall modes have been quenched, $\Theta_{max}(t) = 0$ and $\Theta_0 = 0$, while for modulated wall modes these quantities are not zero. Figure 4 shows the variation in Θ_0 for varying A at $\Omega_m = 10^{1.75}$. Clearly seen is the $\sqrt{A_c - A}$ scaling characteristic of a Hopf bifurcation while the measured Hopf frequencies $\Omega_H(A)$ vary weakly between 4.7807 and 4.8447 for $\Theta_0 > 0$; $\Omega_H = 4.8127$ for the unmodulated case $A = 0$. Figure 5(a) shows how this local (in space and in time) measure of the temperature varies with Ω_m and A for $Ra = 5 \times 10^4$ and $\Omega_0 = 625$. There is a drop in Θ_0 for a range of frequencies centred about $\Omega_m = 10^{1.75}$ that expands with increasing A, and quenching ($\Theta_0 \to 0$) occurs for $A > 0.01$ in this range of frequencies. At low Ω_m, there is an enhancement in Θ_0 with increasing A, but this is an artefact of the phase of the modulation chosen to define Θ_0. While Θ_0 is definitive in characterizing quenching, a more global measure is also needed to assess the net effects of the modulations.

Such a global measure is the time-averaged heat flux across the layer. The heat flux vertically across the layer is characterized by the Nusselt number, the ratio

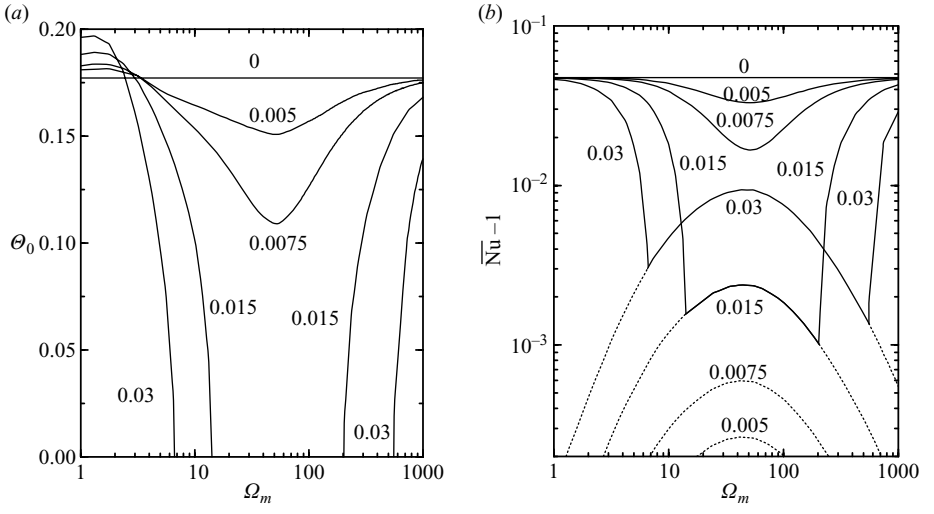

FIGURE 5. Variation with Ω_m of (*a*) Θ_0 and (*b*) $\overline{Nu}-1$, at A as indicated, for modulated wall modes at $Ra = 5\times10^4$ and $\Omega_0 = 625$. The values of $\overline{Nu}-1$ for the axisymmetric synchronous state are drawn as dotted lines in (*b*).

between the heat transfer of the solution considered, and the heat transfer of the $A = 0$ conductive state, given by

$$Nu = -\langle \partial T/\partial z\rangle|_{z=0.5} = \langle 1 - \partial\Theta/\partial z\rangle|_{z=0.5}, \tag{4.2}$$

where $\langle\cdot\rangle = \int_0^\gamma \int_0^{2\pi} \cdot r\,\mathrm{d}r\,\mathrm{d}\theta$. Since the flow is time dependent for $A > 0$, we consider the Nusselt number averaged over the modulation period τ

$$\overline{Nu} = \frac{1}{\tau}\int_0^\tau Nu\ \mathrm{d}t. \tag{4.3}$$

Note that for $A = 0$, since the wall modes are rotating waves whose spatial structure simply precesses without change, their Nusselt number is constant.

Figure 5(*b*) shows that the mean heat flux associated with the modulated wall modes is diminished with increasing A. For the range of Ω_m for which the wall modes are quenched ($\Theta_0 \to 0$), the system is not convecting heat in the usual sense, however, the synchronous state to which the modulated wall modes are quenched have $\overline{Nu}-1 \neq 0$. This modulation-driven heat flux is considerably smaller than that in the absence of modulation with all other parameters being equal, as evidenced in figure 5(*b*). For values of Ω_m and A for which quenching does not occur, we have also computed the (unstable) synchronous state by restricting the simulations to the axisymmetric subspace, i.e. solving the axisymmetric governing equations. The corresponding $\overline{Nu}-1$ values are drawn as dotted lines in figure 5(*b*). The points where the solid $\overline{Nu}-1$ curves of the modulated wall modes meet these dotted curves (for the same value of A) correspond to symmetry-restoring Hopf bifurcations responsible for the quenching. For the range of Ω_m where quenching takes place, the heat flux $\overline{Nu}-1$ peaks to non-trivial values. This enhanced heat flux is driven by the oscillatory boundary layers. This mechanism is explored in the following subsection.

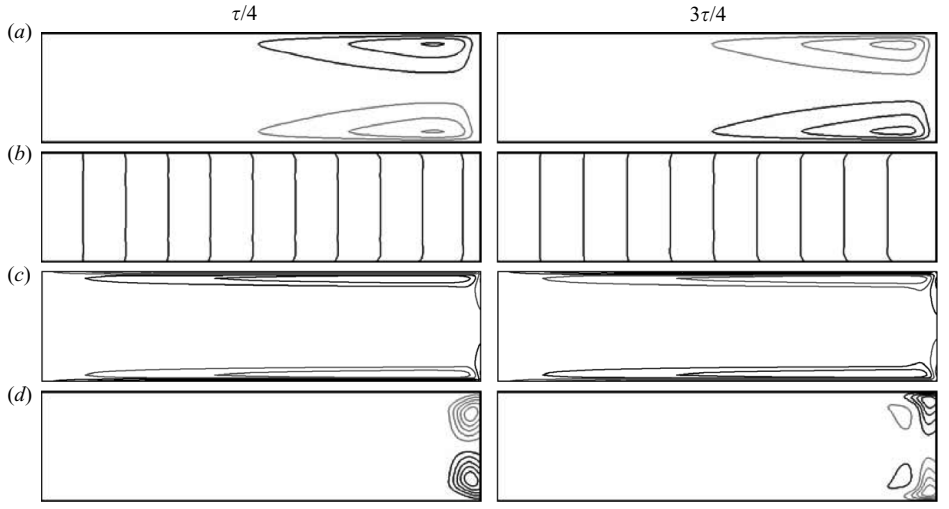

FIGURE 6. Contours in a meridional plane $r \in [0, \gamma]$, $z \in [-0.5, 0.5]$ of (*a*) ψ (streamlines), (*b*) $rv + r^2\Omega_0$ (vortex lines), (*c*) η (azimuthal vorticity) and (*d*) Θ (temperature perturbation), for the synchronous state at $A = 0.05$, $\Omega_m = 10^{1.75}$, $Ra = 4 \times 10^4$ and $\Omega_0 = 625$. Five positive (black) and five negative (grey) contours are linearly spaced for $\psi \in [-1.5, 1.5]$ and $\Theta \in [-0.1, 0.1]$, five positive and five negative contours are quadratically spaced for $\eta \in [-1000, 1000]$, while 10 contours are quadratically spaced for $rv + r^2\Omega_0 \in [0, 1 \times 10^4]$. Movie 4, available in the online version, shows this solution over 1.12 viscous times (10 modulation periods) at a rate of 0.0186 viscous times per second (6 s per modulation period).

4.2. *Synchronous state*

In order to better understand the interaction between the oscillating boundary layers and the wall-localized thermal plumes, it is useful to study the boundary layers in isolation from the wall modes in the synchronous state. Since the synchronous state is axisymmetric, it is convenient to describe it in terms of streamlines and vortex lines. In the laboratory frame, the velocity is $(u, v + r\Omega_0, w)$, and the meridional components can be written in terms of the Stokes stream function $u = -1/r\partial\psi/\partial z$ and $w = 1/r\partial\psi/\partial r$. The corresponding vorticity is

$$\left(-\frac{1}{r}\frac{\partial(rv + r^2\Omega_0)}{\partial z}, -\frac{1}{r}\left(\frac{\partial^2}{\partial r^2} - \frac{1}{r}\frac{\partial}{\partial r} + \frac{\partial^2}{\partial z^2}\right)\psi, \frac{1}{r}\frac{\partial(rv + r^2\Omega_0)}{\partial r}\right). \tag{4.4}$$

Contours of ψ in a meridional plane depict the streamlines, and likewise, contours of $rv + r^2\Omega_0$ depict the vortex lines. Note that since Ω_0 is a constant, the radial vorticity is simply $-\partial v/\partial z$. The only variables that change between the laboratory and the rotating reference frames are the azimuthal component of velocity (differs by $r\Omega_0$) and the vertical vorticity (differs by the constant term $2\Omega_0$).

In the unmodulated problem, for $Ra < Ra_c$ the fluid remains in solid-body rotation with vortex lines parallel to the rotation axis. For $A > 0$, the vortex lines are alternately displaced radially outward and inward in harmonic Ekman layers at the top and bottom of the cylinder as the cylinder accelerates and decelerates over the modulation period. Of course, the vortex lines are not bent purely in the radial direction, but also into the azimuthal direction (Davidson 1989; Lopez 1995), and this resultant azimuthal component of vorticity η drives a meridional circulation characterized by the stream function $\eta = u_z - w_r = -\psi_{rr}/r + \psi_r/r^2 - \psi_{zz}/r$ (see (4.4)). Figure 6 shows the streamlines, vortex lines, azimuthal vorticity and temperature perturbation of a

periodic solution at $A = 0.05$, $\Omega_m = 10^{1.75}$, $Ra = 4 \times 10^4$ and $\Omega_0 = 625$ at two phases of the modulation period, corresponding to the maximum and minimum values of $\Omega(t)$. Movie 4 in the online version shows the solution in figure 6 over 10 periods. In this case, Ra is well below critical for the onset of thermal convection, ensuring that the synchronous state, which lacks thermally driven convection, is stable. The $\tau/4$ phase of the modulation is the end of the acceleration phase, and the vortex line bending drives a secondary flow which centrifuges fluid in the harmonic Ekman layers radially outwards. This centrifuged fluid drives cold fluid from the top layer and warm fluid from the bottom layer into the sidewall layer. The harmonic Ekman layers are seen as thin sheets of azimuthal vorticity at the top and bottom lids with weaker layers of oppositely signed vorticity just below and above, respectively. The $3\tau/4$ phase is the end of the deceleration phase; now the vortex lines bend in the reversed direction driving a secondary flow which draws fluid from near the sidewall radially inward in thin harmonic Ekman layers in which the sign of the azimuthal vorticity has changed since the acceleration phase. Fluid from the core moves towards the corners where the lids meet the sidewall to replace the fluid drawn into the harmonic Ekman layers, making the top (bottom) corner relatively warmer (cooler).

Figure 7(a) shows vertical profiles of the azimuthal vorticity at $r = \gamma/2$. For $\Omega_m < 10^{2.5}$, the azimuthal vorticity profiles behave as a standing wave with no noticeable penetration of the azimuthal vorticity beyond $0.15d$ from the lid. The standing waves are predicted by the analysis of simple-harmonic Ekman flow (Chapter 7, § 3.5 of Yih 1977), which considers the harmonic modulation of a rotating infinite disk, at vertical location $z^* = 0$ with length scale $\sqrt{\nu/\Omega_0}$, where Ω_0 is the mean rotation equal to the background rotation. Such a flow has an azimuthal velocity

$$v(z^*, t) = 0.5A\Omega_0 \mathrm{Re}\left[\mathrm{e}^{-\beta_1 z^* + \mathrm{i}\Omega_m t} + \mathrm{e}^{-\beta_2 z^* + \mathrm{i}\Omega_m t}\right], \tag{4.5}$$

where Re denotes the real part and β_1 and β_2 are the roots with positive real part of the characteristic polynomial that arises after the radial velocity is eliminated

$$y^4 - \mathrm{i}2\Omega_m y^2 - \left(\Omega_m^2 - 4\Omega_0^2\right) = 0. \tag{4.6}$$

The arrows shown with the azimuthal vorticity in figure 7(a) show the characteristic scaling lengths $\delta_{\beta_1} = \mathrm{Re}(\beta_1)^{-1}$ and $\delta_{\beta_2} = \mathrm{Re}(\beta_2)^{-1}$ for each Ω_m. When $\Omega_m < 2\Omega_0$, the solution is a pair of counter-propagating waves that are nearly balanced for small modulation frequencies. When $\Omega_m/\Omega_0 << 1$, Yih's solution can be approximated by

$$v(z^*, t) \approx A\Omega_0 \mathrm{e}^{-\Omega_0^{-0.5} z^*} \cos(\Omega_m t) \cos\left(2\Omega_0^{0.5} z^*\right), \tag{4.7}$$

which is a standing wave. For $\Omega_m \geqslant 10^{2.5}$, the two theoretically predicted counter-propagating waves are no longer nearly balanced and the azimuthal vorticity near the top and bottom lids act as travelling waves. Figure 7(b) shows radial profiles of the relative axial vorticity $v/r + v_r$, at the mid-height $z = 0$. For the range of modulation frequencies explored, the sidewall boundary layer behaves as a travelling wave similar to a Stokes layer, whose $\delta_{St} = \Omega_m^{-0.5}$ scaling depth is shown in the figure for each sidewall relative axial vorticity profile.

The depth of the boundary layer at the top and bottom lids was estimated by finding the first zero of the azimuthal vorticity (circles in figure 7a). The results are shown in figure 8(a) and are compared with the harmonic Ekman layer depths δ_{β_1} and δ_{β_2} given by Yih (1977), which we have scaled to the mean boundary layer depth in our problem at $\Omega_m = 1$. The theoretical estimates of Yih capture the Ω_m dependence of our boundary layers on the top and bottom lids, including the onset and approximate

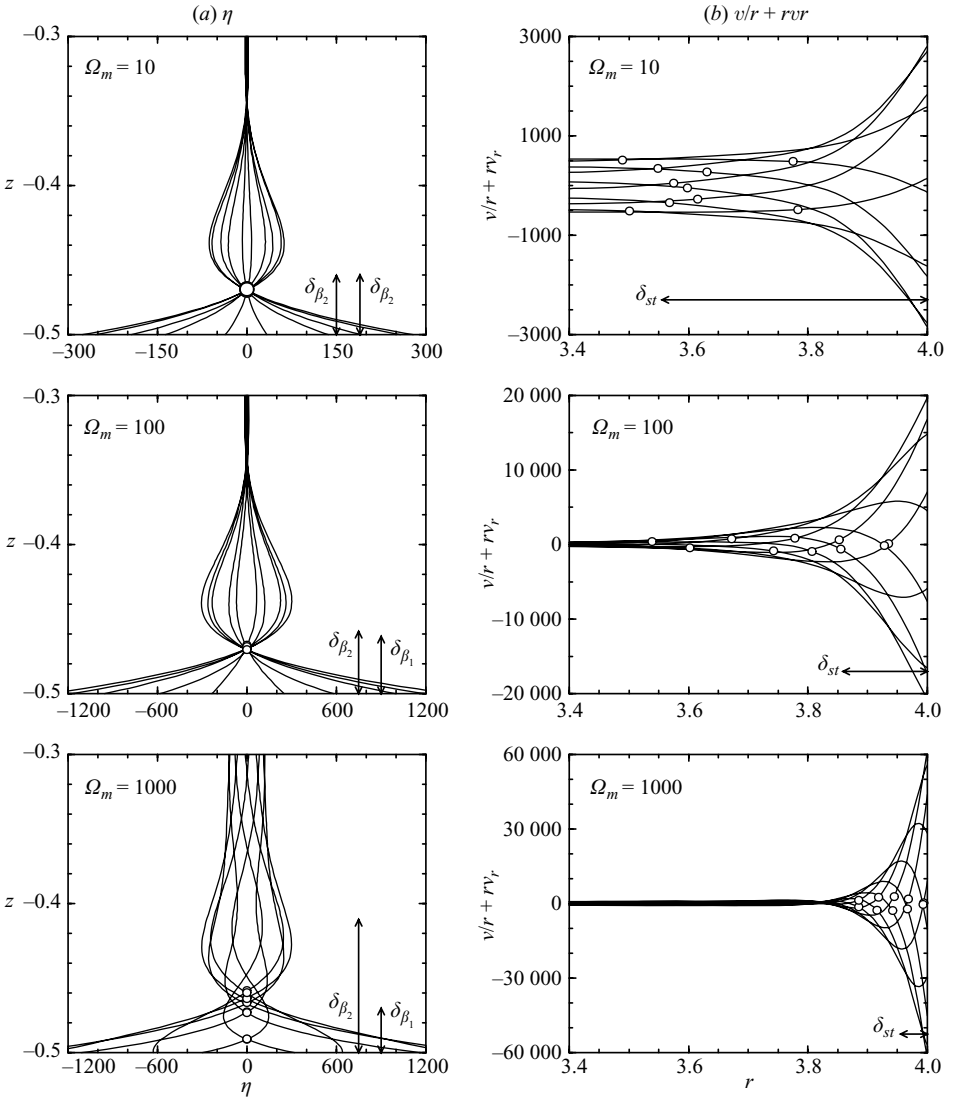

FIGURE 7. Profiles of η (azimuthal vorticity) and $v/r + rv_r$ (relative axial vorticity) for the synchronous states at $A = 0.05$, $Ra = 4 \times 10^4$, $\Omega_0 = 625$ and various Ω_m. Data is shown at $r = \gamma/2$ for $z \in [-0.5, -0.25]$ and $r \in [3.4, 4.0]$, respectively, over 10 equally spaced phases of a modulation period. The circles show the boundary layer depth estimate for each time that is used in the calculation in figure 8. The arrows labelled δ_{β_1} and δ_{β_2} give the boundary layer depth estimates for Yih's harmonic Ekman layer analysis in the vertical azimuthal vorticity figures and the arrows labelled δ_{St} give the Stokes boundary layer depth estimate in the radial relative axial vorticity figures.

magnitude of the travelling waves found at higher Ω_m. Measurements of the boundary layer thickness at the sidewall are more difficult as the far-field ($r = 0$) axial vorticity adjusts with the modulation. The sidewall boundary layer depth was estimated as the distance where the relative axial vorticity near the sidewall is 90 % of its free stream value. For $\Omega_m < 10$ the mean boundary layer depth is approximately independent of Ω_m, whereas for larger Ω_m, it has the classical Stokes layer scaling of $\Omega_m^{-0.5}$. At

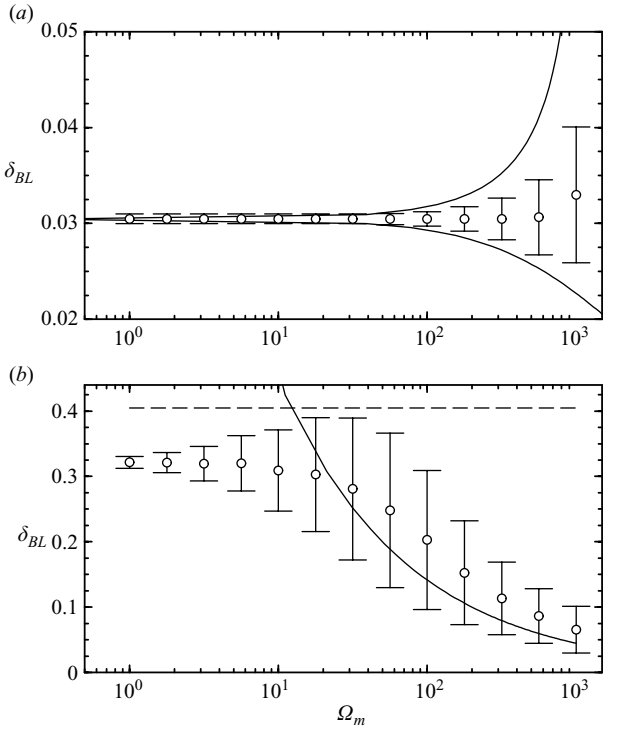

FIGURE 8. (*a*) Estimated top and bottom lids boundary layer depth δ_{BL} for synchronous states at $A = 0.05$, $Ra = 4 \times 10^4$, $\Omega_0 = 625$ and various Ω_m at $r = \gamma/2$ over a modulation period. δ_{β_1} and δ_{β_2}, the theoretical harmonic Ekman layer depth estimate given by Yih and scaled to the measurement at $\Omega_m = 1$ are shown as solid lines, forming a horn-shaped region. (*b*) Estimated sidewall boundary layer width measured at $z = 0$ for the same cases as shown in (*a*). A solid line indicates the theoretical Stokes layer depth estimate and a dashed line indicates the width of a thermal plume in the unmodulated case. In both plots mean values are shown as empty circles with the standard deviation denoted by error bars.

frequencies near optimal for quenching wall modes, the variation of its depth over a period (characterized by the standard deviation, as indicated by the error bars in the figure) is largest, tapering off for larger and smaller Ω_m.

For the synchronous state, the instantaneous (u, v, w, Θ) scale linearly with A. Figure 9(*a*) illustrates this linear scaling by plotting the L_2-norms of $(u, v, w, \Theta)/A$ at a particular phase of the modulation period ($t_0 = \tau/2$), for $Ra = 4 \times 10^4$ and $\Omega_0 = 625$ over a range of Ω_m and several values of A. Similar linear scalings with A occur at other phases. For larger A the linear scaling deteriorates slightly; this is manifested as a phase shift in the instantaneous azimuthal velocity v.

The time averages over a modulation period of (u, v, w, Θ) scale with A^2. Figure 9(*b*) illustrates this by plotting the L_2-norms of $(\overline{u}, \overline{v}, \overline{w}, \overline{\Theta})/A^2$, where

$$(\overline{u}, \overline{v}, \overline{w}, \overline{\Theta}) = \frac{1}{\tau} \int_0^\tau (u, v, w, \Theta)(r, \theta, z, t)\, \mathrm{d}t. \tag{4.8}$$

The difference between the linear scaling for the instantaneous fields and the quadratic scaling for the time averages can be accounted for by considering the Fourier expansions of the variables in time. Since the synchronous axisymmetric state is time periodic with the same period as the forcing $\tau = 2\pi/\Omega_m$, it can be Fourier

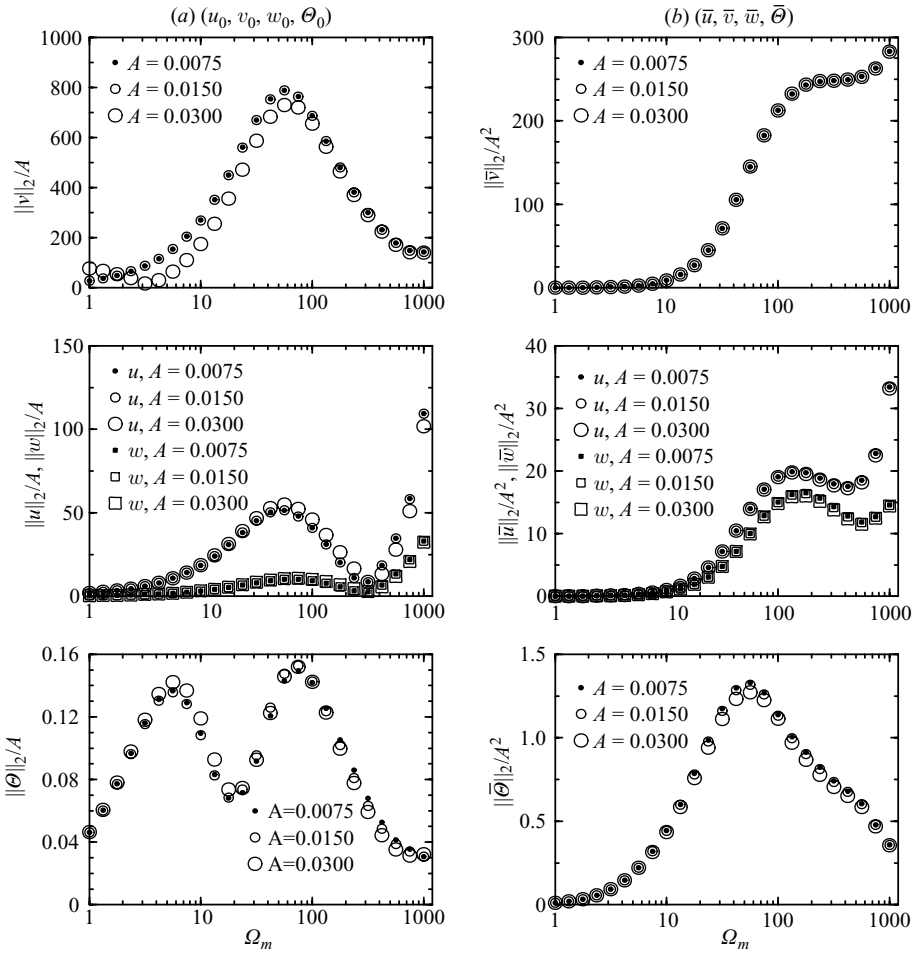

FIGURE 9. Variations with A and Ω_m of (a) the L_2-norms of $(u_0, v_0, w_0, \Theta_0)$ divided by A for $A = 0.0075, 0.0150, 0.0300$ and (b) the L_2-norms of the $(\overline{u}, \overline{v}, \overline{w}, \overline{\Theta})$ divided by A^2 for $A = 0.0075, 0.0150, 0.0300$, both taken for synchronous states with $Ra = 4 \times 10^4$, $\Omega_0 = 625$.

expanded in time as (using v as an example)

$$v(r, z, t) = \sum_{n=-\infty}^{\infty} C_n(r, z) \mathrm{e}^{\mathrm{i}n\Omega_m t} . \tag{4.9}$$

Substitution into the Navier–Stokes equations results in a coupled system of PDEs for the coefficients $C_n(r, z)$. The equation for C_n is linear, except for the advection terms which are quadratic and couple Fourier modes with different n. The external forcing appears only in the boundary conditions for the $n = 1$ mode. As a result, for small forcing amplitude A (so that higher order terms coming from the nonlinearities are smaller than the boundary forcing, which is linear in A), $C_1 \propto A$. This is the origin of the linear scaling of the instantaneous velocity with A. The source terms for the $n \neq 1$ temporal Fourier modes come exclusively from the quadratic advection terms, resulting in $C_0, C_2 \propto A^2$, $C_3 \propto A^3$ and so on (in fact, $C_n \propto A^n$ for $n \geqslant 1$, where A^n is the lowest order of A appearing in C_n). Upon taking time averages of a periodic

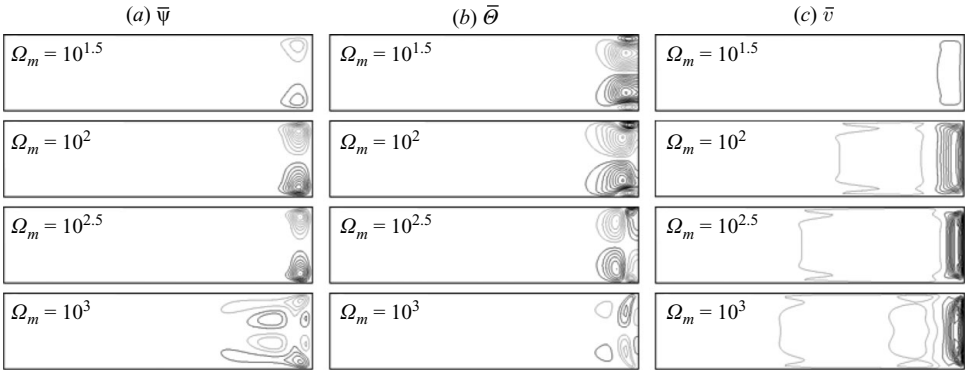

FIGURE 10. Contours of the meridional streaming flow $\overline{\Psi}$, mean temperature perturbation $\overline{\Theta}$ and azimuthal streaming flow $\overline{v}$, for synchronous states at $A = 0.03$, $Ra = 4 \times 10^4$, $\Omega_0 = 625$ and various Ω_m. Ten positive (black) and 10 negative (grey) contours are linearly spaced for $\overline{\Psi} \in [-0.03, 0.03]$, $\overline{\Theta} \in [-0.01, 0.01]$ and $\overline{v} \in [-1.5, 1.5]$, in a meridional plane $r \in [0, \gamma]$, $z \in [-0.5, 0.5]$.

quantity, such as v, only the zero Fourier mode survives, because

$$\int_0^\tau \mathrm{e}^{\mathrm{i}n\Omega_m t}\,\mathrm{d}t = 0, \quad \forall\, n \neq 0. \tag{4.10}$$

Therefore $\overline{v} \propto C_0 \propto A^2$, giving the observed quadratic scaling with A. In summary, instantaneous values are dominated by the $n = 1$ temporal Fourier mode, driven by the forcing, with amplitude proportional to A, while the time-averaged values contain only the $n = 0$ Fourier mode, driven by the quadratic advection terms, with amplitudes proportional to A^2.

The mean streaming flow characterized in figure 9(b) is driven by the modulations. It is negligible for $\Omega_m < 10$, and the mean meridional flow has a relative maximum near $\Omega_m = 100$. The L_2-norm of the mean azimuthal flow is an order of magnitude larger than that of the mean meridional flow, and all the mean velocity components are largest at the highest frequencies considered. The mean thermal perturbation is largest near the optimal quenching frequency of $\Omega_m = 10^{1.75}$ and gradually declines with increasing Ω_m. This is consistent with the behaviour of $\overline{Nu} - 1$, the time-averaged Nusselt number, discussed in § 4.1, since

$$\overline{Nu} \;= < 1 - \partial\overline{\Theta}/\partial z >_{z=0.5}\,. \tag{4.11}$$

The structure of the mean streaming flow, which is axisymmetric, in a meridional plane at $A = 0.05$, $Ra = 4 \times 10^4$ and $\Omega_0 = 625$, for various Ω_m, is shown in figure 10. The streaming flow is strongest near the sidewall, occupying about the same volume as the thermal plumes of the wall mode at the higher $Ra = 5 \times 10^4$. The mean meridional flow, characterized by the mean stream function, is shown in figure 10(a). At the highest frequencies, the mean meridional flow penetrates into the interior. The structure of the mean thermal perturbation $\overline{\Theta}$ is shown in figure 10(b). Figure 10(c) shows the mean azimuthal flow $\overline{v}$, which is in the prograde direction, whereas the unmodulated wall mode precesses in the retrograde direction.

From the parametric studies of the wall-mode quenching and of the structures of the boundary layers and the mean flow, three different frequency regimes clearly emerge. The *low-frequency regime* corresponds to frequencies $\Omega_m \lessapprox 10^{0.5}$ for the $Ra = 4 \times 10^4$ and $\Omega_0 = 625$ case shown in detail in this section. In this regime, the harmonic

Ekman layers at the top and bottom endwalls behave as standing waves. The sidewall boundary layer is thick, its depth varies little in time, and the mean streaming flow $(\overline{u}, \overline{v}, \overline{w}, \overline{\Theta})$ is very weak.

The *intermediate-frequency regime*, where the quenching acts efficiently, corresponds to frequencies $10^{0.5} \lessapprox \Omega_m \lessapprox 10^{2.5}$ for the $Ra = 4 \times 10^4$ and $\Omega_0 = 625$ case. Here, the harmonic Ekman layers at the top and bottom endwalls continue to behave as standing waves, the sidewall boundary layer is also thick, but its depth varies considerably with time. The magnitude of the azimuthal mean velocity increases with frequency in this regime. The magnitudes of the mean meridional velocities have local maxima for Ω_m very close to the most efficient quenching frequency, and the magnitude of $\overline{\Theta}$ is also largest in this frequency range. This strongly suggests that the physical mechanism responsible for the quenching is associated with the strong meridional mean flow and the corresponding enhanced heat transport. This meridional mean flow is localized near the sidewall, where the thermal plumes of the wall modes also appear. The spatial structure of this mean flow is in sharp contrast to the structure of the thermal plumes of the wall modes. The mean flow is axisymmetric and reflection symmetric with respect to the horizontal mid-plane, and its vertical velocity and temperature perturbation change sign in the top and bottom halves of the cylinder, vanishing at mid-height. The wall mode thermal plumes are far from axisymmetric and have maximum vertical velocity at mid-height, and this changes sign from plume to plume in the azimuthal direction, with the cold plumes comprised of descending fluid and the hot plumes with rising fluid.

The *high-frequency regime* corresponds to frequencies larger than about $\Omega_m \approx 10^{2.5}$ (for the $Ra = 4 \times 10^4$ and $\Omega_0 = 625$). In this regime, the harmonic Ekman layers behave as travelling waves and the sidewall boundary layer is thin and its depth varies little with time. The magnitudes of mean velocities are larger than in the intermediate-frequency regime, while the mean temperature $\overline{\Theta}$ is smaller. The quenching mechanism ceases to work, very likely because the meridional mean flow is no longer concentrated at the sidewall boundary layer but penetrates into the bulk, and the induced heat transport decreases. The salient feature in this regime is the presence of a very strong azimuthal steady streaming, which drags the thermal plumes reducing their precession frequency.

We have defined the frequency ranges in the particular case $Ra = 4 \times 10^4$ and $\Omega_0 = 625$ discussed in detail in the paper. They can be defined in other parameter regimes in terms of the frequency at which the mean temperature $\overline{\Theta}$ reaches its maximum value, Ω_m^{max} (see figure 10*b*). The intermediate-frequency regime is centred around this Ω_m^{max} frequency, and it extends approximately 1 order of magnitude below and above this value.

4.3. *Modulated wall modes*

For modulation frequencies and amplitudes where the wall modes are not quenched, the behaviour of the resultant modulated wall modes are characterized by two regimes, the low and the high Ω_m regimes described above. For amplitudes A where there is no quenching for any Ω_m, there is a smooth transition between these two regimes. However, for A large enough (greater than about 1 %), the two regimes are well separated by a spectral gap in Ω_m which grows with A (see figure 5).

Figures 11(*a*) and 11(*b*) show an overhead and perspective view of a modulated wall mode with $A = 0.0075$, $\Omega_m = 10^{1.75}$, $Ra = 5 \times 10^4$ and $\Omega_0 = 625$ at the beginning of a modulation period. While the wavenumber and overall shape of the plumes remain intact, Θ_0 is about half that of the unmodulated wall mode shown in figure 2(*a*).

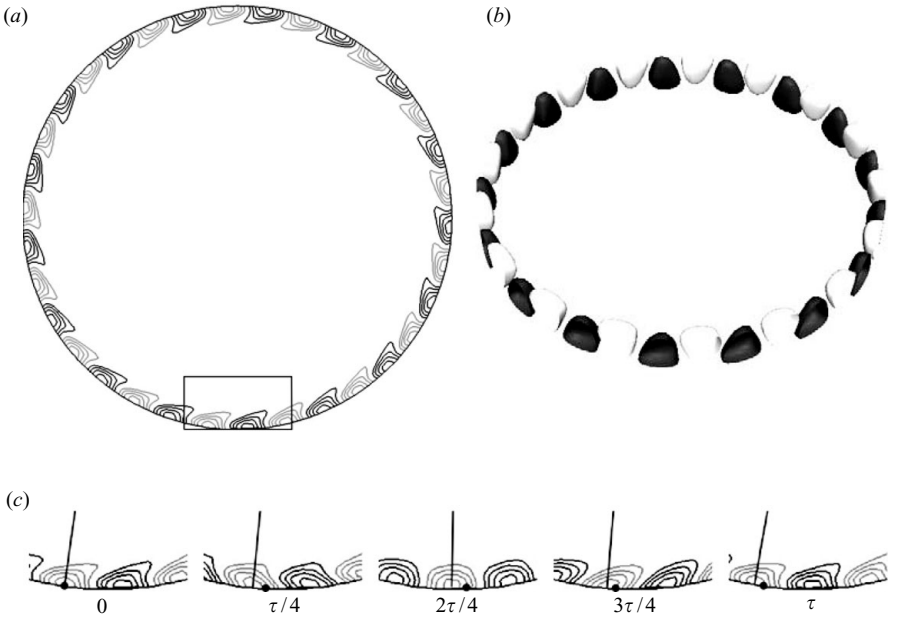

FIGURE 11. (*a*) Temperature perturbation Θ at the start of a modulation period for $A = 0.0075$, $\Omega_m = 10^{1.75}$, $Ra = 5 \times 10^4$ and $\Omega_0 = 625$; it shows contours at $z = 0$, five positive (black) and five negative (grey) in the range $\Theta \in [-0.125, 0.125]$, (*b*) a perspective view of isosurfaces at $\Theta = \pm 0.05$. (*c*) Close ups of the horizontal section delineated by the box in (*a*) over a modulation period τ; the black radial line in each frame indicates the centre of a single cold plume over time and a black dot on the cylinder wall shows the position of a fixed point on the boundary.

At this low-modulation amplitude ($A = 0.0075$), the secondary flow driven by the oscillatory boundary layers co-exists with the wall-localized plumes. At $\Omega_m = 10^{1.75}$, the plumes do not precess significantly over the course of a modulation period. Figure 11(*c*) shows the temperature perturbation at mid-height $z = 0$ in a horizontal section near the sidewall (indicated by the box in figure 11*a*). The radial line in each panel of figure 11(*c*) indicates the angular location of an individual cold plume and the black dot on the cylinder wall indicates the modulated rotation of the cylinder.

In the low Ω_m regime (with periods much larger than the thermal adjustment time, d^2/κ) and low-modulation amplitudes ($A < 0.01$), the wall mode adjusts quasi-statically between states with Coriolis numbers $\Omega_0(1 \pm A)$. The adjustment in the precession rate lags the change in the cylinder rotation by a small percentage of the modulation period. Figure 12(*a–c*) shows space–time diagrams of $\Theta(r = \gamma, \theta, z = 0, t)$ over 10 viscous times for low $\Omega_m = 10^{0.5}$ at various A. The plots are presented in the reference frame of the modulated cylinder, as the convective plumes are advected by the velocity fields in the sidewall boundary layer, complicating the use of the constant rotation frame for low-modulation frequencies as the position of the cylinder can deviate by as much as $2A\Omega_0/\Omega_m$ radians from its original position in the reference frame rotating at the mean rotation rate. For low Ω_m, solutions with increasing A have significantly larger angular displacements, indicating that the azimuthal velocity near the sidewall is out of phase with the modulation. The convection is periodically enhanced during the acceleration phase and impeded during the deceleration phase of the modulation (seen as higher and lower contrasts in grey scale of the diagrams).

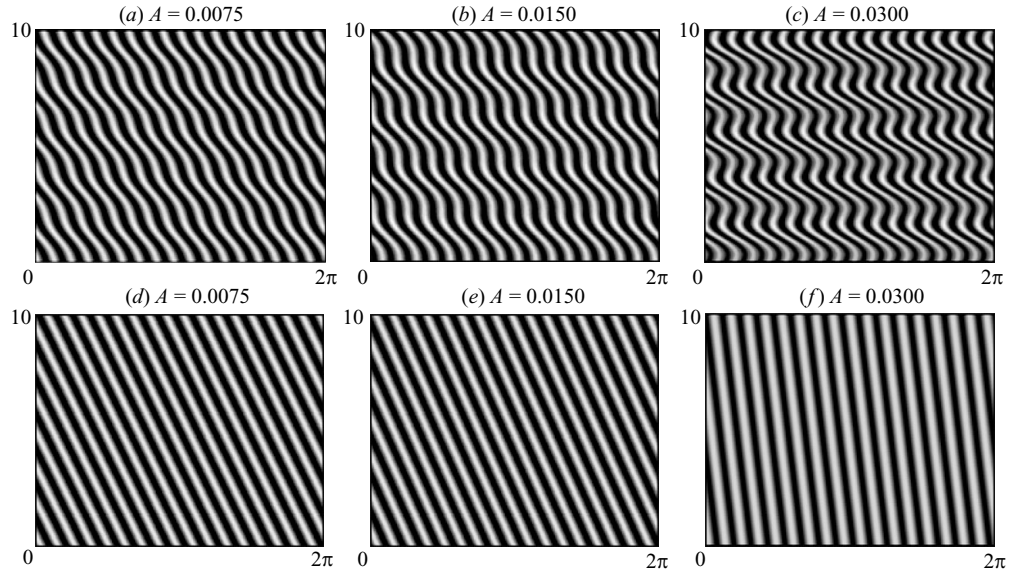

FIGURE 12. Space–time diagrams of modulated wall modes at $Ra = 5 \times 10^4$ and $\Omega_0 = 625$, showing $\Theta(r = \gamma, \theta, 0, t)$ with $\theta \in [0, 2\pi)$ (horizontal) in the reference frame of the modulated cylinder over 10 viscous times (vertical), for various A in (a–c) the low-frequency regime with $\Omega_m = 10^{0.5}$ and in (d–f) the high-frequency regime with $\Omega_m = 10^3$. A little over five modulations periods are shown for $\Omega_m = 10^{0.5}$ and almost 1600 modulation periods are shown for $\Omega_m = 10^3$.

The high $\Omega_m = 10^3$ space–time diagrams are shown in figure 12(d–f). On the scale of the figures, the high-frequency modulation is not visible; in the time shown (10 viscous times) there are about 1600 modulation periods. For $A = 0.0075$, the space–time diagram is virtually indistinguishable from that of the unmodulated wall mode; the mean precession is virtually the same as Ω_p. For large Ω_m, increasing A has the effect of slightly weakening the convection while substantially changing the pattern precession rate; the net precession at $A = 0.03$ has been slowed down considerably.

Figure 13 shows the angular position of the centre of a plume over 10 modulation periods for $A = 0.0075$, 0.0150 and 0.0300 with $\Omega_m = 10^3$, $Ra = 5 \times 10^4$ and $\Omega_0 = 625$. The plumes are sloshed back and forth by the modulation, and the amplitude of this sloshing motion increases linearly with A, as with the instantaneous velocity fields of the synchronous state. A solid black line gives the angular position of the centre of a plume for the unmodulated case at the same Ra and Ω_0. The net precession of an individual plume over a modulation period can be quantified by $\overline{\Omega_p} = (\phi_f - \phi_i)/\tau$, where ϕ_i and ϕ_f are the initial and final angular positions of a plume over a modulation period τ; at $A = 0$, $\overline{\Omega_p} = \Omega_p$. The symbols in figure 13 correspond to the angular position of the plume at the end of each period. These symbols are on straight dashed lines of slope $\overline{\Omega_p}$. The change in the net precession with increasing modulation amplitude A is quadratic, as is the mean velocity field of the synchronous state.

For $\Omega_m < 10^{1.75}$, $\overline{\Omega_p}$ is approximately equal to the precession rate of the unmodulated wall mode. However, for larger Ω_m, the mean precession rate slows, stops and reverses with increasing A; figure 14 gives the variation of $\overline{\Omega_p}$ with A for three different values of Ω_m. The contribution of the mean azimuthal streaming flow

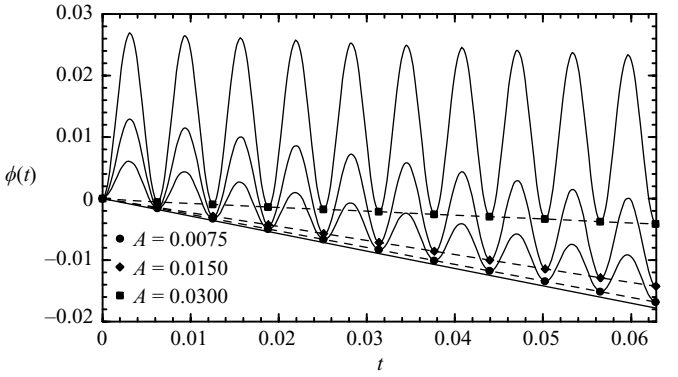

FIGURE 13. Angular position of the centre of a plume over 10 periods for A as indicated; the symbols correspond to the angular position of the plume at the end of each period. $\Omega_m = 10^3$, $Ra = 5 \times 10^4$ and $\Omega_0 = 625$. A black line indicates the angular position of the centre of a plume for the unmodulated case at the same Ra and Ω. Dashed lines show $\overline{\Omega}_p t$ for each solution.

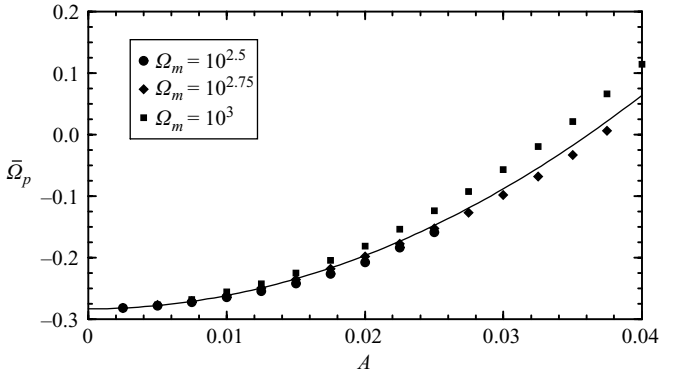

FIGURE 14. Variation of $\overline{\Omega_p}$ with A for Ω_m as indicated. The solid line shows the maximum mean angular velocity for synchronous states at $\Omega_m = 10^3$, $Ra = 4 \times 10^4$, $\Omega_m = 625$, translated by the precession frequency of the unmodulated wall mode Ω_p.

(figure 10) in advecting the thermal plumes at high Ω_m is quantified by the solid line in figure 14. This line corresponds to the maximum mean angular velocity $||\overline{v}/r||_\infty$ of the synchronous state at $\Omega_m = 10^3$, $Ra = 4 \times 10^4$, $\Omega_0 = 625$ plus the retrograde (negative) precession frequency of the unmodulated wall mode Ω_p. The variation in $\overline{\Omega_p}$ with A is mostly accounted for by the angular velocity associated with the azimuthal streaming flow induced by the high-frequency modulations.

5. Conclusions

We have considered rotating Rayleigh–Bénard convection in a regime where the rotation (characterized by the Coriolis number Ω_0) is sufficiently larger than the onset of thermal convection, as the Raleigh number Ra is increased, is to a wall mode consisting of a pattern of hot and cold plumes, localized in the cylinder sidewall boundary layer, that precesses retrograde to the background rotation. These wall modes have been subjected to harmonic modulations of the rotation rate of very small amplitude A and over a wide range of modulation frequencies Ω_m. The

modulation gives rise to oscillatory boundary layers on the top, bottom and side endwalls of the cylinder which drive a large-scale axisymmetric oscillatory flow, and for medium and high frequencies they also drive a mean streaming flow, both of which are strongest at the cylinder sidewall, precisely where the wall-mode plumes are manifest. The nonlinear interactions between the modulation-driven axisymmetric flows and the wall modes have been explored in detail.

The dynamics of the onset of thermal convection in the modulated problem as Ra is increased are qualitatively the same as in the unmodulated case, however, the basic state is now a limit cycle synchronous with the modulation instead of the trivial state of solid-body rotation with a linear temperature profile in z, and the onset of thermal convection is to modulated wall modes at a Hopf bifurcation from the non-trivial basic state. A striking result of the imposed modulations over a wide range of frequencies, even for very small amplitudes, is the delay in the onset of the wall modes to much higher Ra, or for a given Ra, the complete quenching of the wall modes as the modulation amplitude A is increased. This delay of the onset of the wall modes is not a resonance effect, but rather a nonlinear interaction between the oscillatory boundary layers, which are inherently very stable against three-dimensional disturbances, and the wall modes, which are inherently three-dimensional. The lack of resonances when modulating rotating waves follows from the general theory that Hopf bifurcations from rotating waves do not manifest frequency-locking due to the rotational symmetry in the problem (Rand 1982; Krupa 1990). We have observed and analysed the same absence of resonances in harmonically modulated Taylor–Couette flow (Avila *et al.* 2007).

The use of oscillatory Stokes boundary layers in the control of hydrodynamic instabilities has a long history (Davis 1976). They are particularly efficient in inhibiting and quenching three-dimensional instabilities, even when the applied amplitude is very small. We have observed this in diverse flows, including Taylor–Couette (Marques & Lopez 1997, 2000; Avila *et al.* 2007), vortex breakdown (Lopez *et al.* 2008), rotating convection (Rubio *et al.* 2008) and the present flow provides yet another example. The well-defined structure of the wall modes has allowed us in this problem to explore in detail the interactions between the three-dimensional rotating thermal convection flow and the axisymmetric modulation-driven flow.

The nonlinear interaction between the oscillatory boundary layers and the wall modes is characterized by three different frequency regimes. The low Ω_m regime consists of a quasi-static adjustment to wall modes corresponding to the instantaneous value of the background rotation $\Omega(t) = \Omega_0[1 + A\sin(\Omega_m t)]$. In the high Ω_m regime, the thermal plumes associated with the wall mode remain intact despite the much stronger oscillatory and mean flows. However, the strong azimuthal streaming flow, whose strength increases with A and Ω_m, greatly affects the motion of the wall modes, resulting in the thermal plumes precessing in the prograde direction at the largest values of A and Ω_m explored, as shown in figure 14.

For intermediate Ω_m, the action of the oscillatory boundary layers optimally quench the three-dimensional aspects of the flow. This quenching occurs as a symmetry-restoring Hopf bifurcation in which the non-axisymmetric component of the solution associated with thermal convection disappears. There is a large band of modulation frequencies for which the onset of wall-localized thermal convection is delayed by at least 18 % for modulation amplitudes as small as 1 % of the background rotation rate. The physical mechanism by which this delay occurs is characterized by the time-averaged Nusselt number of the synchronous state, and by extension, the strength of the mean thermal perturbation. The effect of the secondary

modulation-driven flow on the thermal field is most pronounced for frequencies near $\Omega_m = 10^{1.75}$, even though the oscillatory and mean velocity are considerably stronger at larger Ω_m for a fixed A. However, the meridional component of the mean streaming flow peaks in strength in the intermediate Ω_m regime, and is seen to be responsible for the quenching. As the strong secondary flow driven by the oscillatory boundary layers is a consequence of the finite geometry of the enclosed cylinder, we have the result of suppressing one confinement effect (wall-localized convection) with another (secondary flow due to the action of the oscillatory boundary layers).

This work was supported by the National Science Foundation grant DMS-0509594, and the Spanish and Catalan government grants FIS2007-61585 and SGR-00024. Rubio was supported by a Fulbright fellowship at UPC (Barcelona, Spain), whose hospitality is warmly appreciated.

REFERENCES

Avila, M., Marques, F., Lopez, J. M. & Meseguer, A. 2007 Stability control and catastrophic transition in a forced Taylor–Couette system. *J. Fluid Mech.* **590**, 471–496.

Bhattacharjee, J. K. 1990 Convective instability in a rotating fluid layer under modulation of the rotating rate. *Phys. Rev.* A **41**, 5491–5494.

Bodenschatz, E., Pesch, W. & Ahlers, G. 2000 Recent developments in Rayleigh–Bénard convection. *Annu. Rev. Fluid Mech.* **32**, 709–778.

Davidson, P. A. 1989 The interaction between swirling and recirculating velocity components in unsteady, inviscid flow. *J. Fluid Mech.* **209**, 35–55.

Davis, S. H. 1976 The stability of time-periodic flows. *Annu. Rev. Fluid Mech.* **8**, 57–74.

Ecke, R. E., Zhong, F. & Knobloch, E. 1992 Hopf-bifurcation with broken reflection symmetry in rotating Rayleigh--Bénard convection. *Europhys. Lett.* **19**, 177–182.

Fornberg, B. 1998 *A Practical Guide to Pseudospectral Methods*. Cambridge University Press.

Goldstein, H. F., Knobloch, E., Mercader, I. & Net, M. 1993 Convection in a rotating cylinder. Part 1. Linear theory for moderate Prandtl numbers. *J. Fluid Mech.* **248**, 583–604.

Goldstein, H. F., Knobloch, E., Mercader, I. & Net, M. 1994 Convection in a rotating cylinder. Part 2. Linear theory for low Prandtl numbers. *J. Fluid Mech.* **262**, 293–324.

Herrmann, J. & Busse, F. H. 1993 Asymptotic theory of wall-attached convection in a rotating fluid layer. *J. Fluid Mech.* **255**, 183–194.

Hughes, S. & Randriamampianina, A. 1998 An improved projection scheme applied to pseudospectral methods for the incompressible Navier–Stokes equations. *Intl J. Numer. Meth. Fluids* **28**, 501–521.

Knobloch, E. 1998 Rotating convection: recent developments. *Intl J. Engng Sci.* **36**, 1421–1450.

Krupa, M. 1990 Bifurcations of relative equilibria. *SIAM J. Math. Anal.* **21**, 1453–1486.

Kuo, E. Y. & Cross, M. C. 1993 Traveling-wave wall states in rotating Rayleigh–Bénard convection. *Phys. Rev.* E **47**, R2245–R2248.

Küppers, G. & Lortz, D. 1969 Transition from laminar convection to thermal turbulence in a rotating fluid layer. *J. Fluid Mech.* **35**, 609–620.

Lopez, J. M. 1995 Unsteady swirling flow in an enclosed cylinder with reflectional symmetry. *Phys. Fluids* **7**, 2700–2714.

Lopez, J. M., Cui, Y. D., Marques, F. & Lim, T. T. 2008 Quenching of vortex breakdown oscillations via harmonic modulation. *J. Fluid Mech.* **599**, 441–464.

Lopez, J. M. & Marques, F. 2004 Mode competition between rotating waves in a swirling flow with reflection symmetry. *J. Fluid Mech.* **507**, 265–288.

Lopez, J. M., Marques, F., Mercader, I. & Batiste, O. 2007 Onset of convection in a moderate aspect-ratio rotating cylinder: Eckhaus–Benjamin–Feir instability. *J. Fluid Mech.* **590**, 187–208.

Lopez, J. M., Rubio, A. & Marques, F. 2006 Traveling circular waves in axisymmetric rotating convection. *J. Fluid Mech.* **569**, 331–348.

Marques, F. & Lopez, J. M. 1997 Taylor–Couette flow with axial oscillations of the inner cylinder: Floquet analysis of the basic flow. *J. Fluid Mech.* **348**, 153–175.

Marques, F. & Lopez, J. M. 2000 Spatial and temporal resonances in a periodically forced extended system. *Phys.* D **136**, 340–352.

Marques, F. & Lopez, J. M. 2008 Influence of wall modes on the onset of bulk convection in a rotating cylinder. *Phys. Fluids* **20**, 024109.

Marques, F., Mercader, I., Batiste, O. & Lopez, J. M. 2007 Centrifugal effects in rotating convection: axisymmetric states and three-dimensional instabilities. *J. Fluid Mech.* **580**, 303–318.

Mercader, I., Net, M. & Falqués, A. 1991 Spectral methods for high order equations. *Comp. Meth. Appl. Mech. Engng* **91**, 1245–1251.

Niemela, J. J., Smith, M. R. & Donnelly, R. J. 1991 Convective instability with time-varying rotation. *Phys. Rev.* A **44**, 8406–8409.

Orszag, S. A. & Patera, A. T. 1983 Secondary instability of wall-bounded shear flows. *J. Fluid Mech.* **128**, 347–385.

Rand, D. 1982 Dynamics and symmetry. Predictions for modulated waves in rotating fluids. *Arch. Ration. Mech. An.* **79**, 1–37.

Riley, N. 2001 Steady streaming. *Annu. Rev. Fluid Mech.* **33**, 43–65.

Rubio, A., Lopez, J. M. & Marques, F. 2008 Modulated rotating convection: radially traveling concentric rolls. *J. Fluid Mech.* **608**, 357–378.

Schlichting, H. 1932 Berechnung ebener periodischer Grenzschichtströmungen. *Phys.* Z **33**, 327–335.

Thompson, K. L., Bajaj, K. M. S. & Ahlers, G. 2002 Traveling concentric-roll patterns in Rayleigh–Bénard convection with modulated rotation. *Phys. Rev.* E **65**, 04618.

Yih, C. 1977 *Fluid Mechanics*. West River Press.

Zhong, F., Ecke, R. E. & Steinberg, V. 1991 Asymmetric modes and the transition to vortex structures in rotating Rayleigh–Bénard convection. *Phys. Rev. Lett.* **67**, 2473–2476.